High Performance Photoluminescent Carbon Dots for In-Vitro and In-Vivo Bioimaging: Effect of Nitrogen Doping Ratios

ARTICLE *in* LANGMUIR · JULY 2015

Impact Factor: 4.46 · DOI: 10.1021/acs.langmuir.5b01875

6 AUTHORS, INCLUDING:

Junqing Wang
The Chinese University of Hong Kong
8 PUBLICATIONS **5** CITATIONS
SEE PROFILE

Pengfei Zhang
guangzhou BoxABIOTECH CO LTD
213 PUBLICATIONS **890** CITATIONS
SEE PROFILE

Ken Cham-Fai Leung
Hong Kong Baptist University
84 PUBLICATIONS **3,107** CITATIONS
SEE PROFILE

Yi-Xiáng Wáng
The Chinese University of Hong Kong
299 PUBLICATIONS **3,599** CITATIONS
SEE PROFILE

30th Anniversary
Langmuir

Article

High Performance Photoluminescent Carbon dots for In-Vitro and In-Vivo Bioimaging: Effect of Nitrogen Doping Ratios

Junqing Wang, Pengfei Zhang, Chao Huang, Gang Liu, Ken Cham-Fai Leung, and Yi-Xiang J. Wang

Langmuir, **Just Accepted Manuscript** • DOI: 10.1021/acs.langmuir.5b01875 • Publication Date (Web): 02 Jul 2015

High Performance Photoluminescent Carbon dots for *In-Vitro* and *In-Vivo* Bioimaging: Effect of Nitrogen Doping Ratios

Junqing Wang,[†,‡] Pengfei Zhang,[‡] Chao Huang,[‡] Gang Liu,[‡] Ken Cham-Fai Leung,*[,§] Yì-Xiáng J Wáng*[,†]

[†]Department of Imaging and Interventional Radiology, Prince of Wales Hospital, The Chinese University of Hong Kong Shatin, NT, Hong Kong SAR (P. R. China)

[‡]State Key Laboratory of Molecular Vaccinology and Molecular Diagnostics & Center for Molecular Imaging and Translational Medicine, School of Public Health, Xiamen University, Xiamen, 361102, P. R. China

[§]Department of Chemistry and Partner State Key Laboratory of Environmental and Biological Analysis, The Hong Kong Baptist University, Kowloon Tong, Kowloon, Hong Kong SAR (P. R. China)

ABSTRACT: Photoluminescent carbon dots (CDs) have received ever-increasing attention in the applications of optical bioimaging because of their low toxicity, tunable fluorescent properties and ultracompact size. We report for the first time on enhanced photoluminescence (PL) performance influence by structure effect among the various types of nitrogen doped (N-doped) PL CDs, these CDs were facilely synthesized from condensation carbonization of linear polyethylenic amine (PEA) analogues and citric acid (CA) of different ratios. Detailed structural and property studies demonstrated that either the structures or molar ratio of PEAs altered the PL properties of the CDs. The content of conjugated π-domains with C═N in carbon backbone was correlated with their PL Quantum Yield (QY) (up to 69%). The hybridization between the surface/molecule state and the carbon backbone were synergistically affecting the chemical/physical properties. Also, long-chain polyethylenic amine (PEA) molecule-doped CDs exhibit increasing photostability but at the expense of PL efficiency, proving that the PL emission of high QY CDs arise not only from the sp^2/sp^3 carbon core and surface passivation of CDs, but also the molecular fluorophores integrated in the CDs. *In-vitro* and *in-vivo* bioimaging of these N-doped CDs showed strong photoluminescence signal. Good biocompatibility demonstrates their potential feasibility for bioimaging applications. In addition, the overall size profile of as-prepared CDs is comparable to the average size of capillary pores in normal living tissues (~5 nm). Our study provides valuable insights into the effects of the PEA doping ratios on photoluminescence efficiency, biocompatibility, cellular uptake, and optical bioimaging of CDs.

1. INTRODUCTION

Various synthetic methods of photoluminescent carbon dots (CDs) have been developed in the past decade, based upon different starting materials. Major synthetic approaches can be divided into 'top-down' and 'bottom-up' routes. The 'top-down' route refers to separating large sized carbon precursors into graphene quantum dots (GQDs), and mostly approached via chemical,[1] electrochemical oxidation,[2] and physical ablation of graphene sheets or carbon nanotubes (CNTs).[3-5] 'Bottom-up' method primarily involves the carbonization and dehydration of non-conjugated small molecules (*e.g.* citric acid, amino acids, carbohydrates *etc.*),[6-8] their emission wavelength and photoluminescence Quantum Yield (PL QY) can be tuned by altering reaction parameters, such as reagent's composition/ratios, reaction time/temperature.[9,10] In general, most PL CDs are abundant of oxygen-containing functional groups that decorated via covalent linkage. Surface passivation and/or doping of other elements, such as nitrogen,[6,7,9,11] phosphorus,[12,13] silicon and sulfur were reported to alter PL properties.[14] Although a variety of methods for fabricating carbon-based nanoparticles were reported, only a few efficient reaction routes were found for high PL QY and high-output CDs preparation. Dong *et al.* reported the synthesis of strong blue fluorescent CDs with 42.5% of QY via low temperature carbonization of branched polyethylenimine and citric acid (CA).[6] Wei and co-workers fabricated a series of multicolor N-doped CDs with PL QY up to 69% through a microwave assisted Maillard reaction from natural amino acids and glucose.[11] Zhu *et al* prepared highly luminescent N-doped CDs with PL QY above 60% at large scale by using ethylenediamine and CA as starting materials through the hydrothermal reaction.[9] The origins of PL from CDs are caused by a variety of determinants that have not been fully understood. Nevertheless, several principles have been proposed that the PL emissions of CDs are generated by quantum confinement effect,[15] the free zigzag sites with triplet carbene at particle edges,[16] spontaneous emission of excitons in surface energy traps through the passivation,[17] and band gap alteration triggered by charge transfer effect.[18] However, most of the PL mechanism studies were based on GQDs, the CDs with higher PL QY that synthesized from small molecules may have quite different mechanisms from GQDs, and the possible causa for such a high PL QY have not been fully investigated. In terms of efficiency for biological application, optimizing PL QY is essential for improving fluorescence signal and consequently reducing the dosage and potential toxicity in bioimaging applications.[19] Here, we initiated a study by aiming the influence of series N-doping agents on optical characteristics and bioimaging performance of N-doped CDs that prepared from three different polyethylenic amine (PEA) molecules, *i.e.*, ethylenediamine (EDA), diethylenetriamine (DETA) and triethylenetetramine (TEPA) with combination of CA in selected ratios at fixed reaction condition.

2. EXPERIMENTAL SECTION

2.1. Materials. Citric acid (CA) anhydrous, ethylenediamine (EDA), diethylenetriamine (DETA), tetraethylenepentamine (TEPA) and Sodium hy-

droxide (NaOH) were purchased from Sigma Aldrich Corporation. All chemicals were used as received without any further purification. Distilled deionized (DDI) water was obtained from a Millipore Milli-Q-RO4 water purification system.

2.2. Preparation of the CD-EDA$_{(2/1)}$, CD-DETA$_{(2/1)}$ and CD-TEPA$_{(2/1)}$. 1.39 mL of EDA / 2.387 mL of DETA / 4.012 mL of DETA and 2 g of citric acid were dissolved in 10 mL of DDI water (see all reaction conditions in Table S3). The solution was subsequently transferred to Teflon-lined stainless autoclave (50 mL) and ran the reactor program at 200 ºC for 6 h. Then the reactors were cooled to room temperature. Afterwards, The yellow/brown/black product solution was neutralized by the addition of NaOH solution and was then dialyzed for 24 h with a dialysis membrane (MWCO 2000 Da from Sigma-Aldrich) to remove the excess salts and reagents. After the product solution was dried to remove water and other small molecules by rotary evaporator at 70 °C, the sample was further dried by vacuum oven at 60 °C for 4 h to obtain the final product with a yield of 45.3% (**CD-EDA$_{(2/1)}$**) / 47.8% (**CD-DETA$_{(2/1)}$**) / 42.4% (**CD-DETA$_{(2/1)}$**). The as-prepared CD was collected in a 25 mL glass sample bottle (Figure S12).

2.3. Characterization. The transmission electron microscopic (TEM) analyses were performed on FEI-TECNAI G2 S-TWIN TEM, operating at an acceleration voltage of 200 kV. X-ray powder diffraction measurements were investigated by Bruker D8 Advance diffractometer through non-monochromatic Cu Kα X-Ray at 40kV, 40mA. X-ray photoelectron spectroscopy (XPS) was performed by SKL-12 spectrometer modified with VG CLAM 4 multichannel hemispherical analyzer. Fourier Transform Infrared (FTIR) spectra of CDs were recorded on Perkin-Elmer Paragon 1000 FTIR spectrometer. Fluorescence spectra, lifetime and quantum yields were measured by the FLS920 Series Fluorescence Spectrometers. Cary UV-300 (Double Beam) Conc. UV-visible spectrophotometer was applied for the UV-Vis absorption measurements of CDs. Zeta Potentials were analyzed on Zetasizer Nano S90 with suitable dilution of samples at room temperature. Surface topology was investigated via an atomic force microscope (AFM) in tapping mode. The carbon structure of the CDs was recorded by Raman spectra on a Renishaw1000 micro-spectrometer with excitation wavelength of 765 nm.

2.4. PL QY measurement. The QY (ϕ) of N-doped CDs was measured by comparative method.[20] Quinine sulfate in 0.1 M H_2SO_4 with a known QY, 0.54[21] was introduced as reference sample and sample (CDs) solutions were dissolved in DI water at varied concentrations. For each sample, UV-Vis absorbance spectrum was recorded and the absorbance at the excitation wavelength used (355 nm) was recorded. Then, PL spectrum of the same solution was measured thereby the integrated PL intensity was calculated. The procedures were repeated at different concentrations and integrated PL intensity *vs* absorbance with linear regression was plotted. Next, absolute values of QY were obtained from the simplified equation (2). Where ϕ is the QY, m is the slope calculated from the linear regression, η is the refractive index of the solvent.

The subscripts *CDs*, *Ref* refer to test sample and reference sample respectively. In addition to the practical measurements, should be noted that UV-Vis absorbance measured at the excitation wavelength should never exceeded 0.1 to avoid the notable self-quenching effect.[22] Excitation/emission slit parameters were always consistent throughout the course of PL measurements.

$$\phi_{CDs} = \phi_{Ref}\left(\frac{m_{CDs}}{m_{Ref}}\right)\left(\frac{\eta^2{}_{CDs}}{\eta^2{}_{Ref}}\right) \quad (1)$$

$$\xrightarrow{(\eta_{CDs} = \eta_{Ref} = 1.33)} \phi_{CDs} = \phi_{Ref}\left(\frac{m_{CDs}}{m_{Ref}}\right) \quad (2)$$

2.5. Cell viability evaluation. The cytotoxicity of the **CD-EDA$_{(2/1)}$**, **CD-DETA$_{(2/1)}$** and **CD-TEPA$_{(2/1)}$** were tested with 3-(4,5-dimethylthiazol-2-yl)-2,5-diphenyl tetrazolium bromide (MTT) method. 100 µL of HeLa cells (5×10^4 cells mL^{-1}) (sine the Hela is the most well-known immortal cervical cancer cell line in existence and have been widely used to investigate the processes involved in the growth, differentiation, and death of cells. Their individual cellular behavior can also be easily observed by optical microscope) for each well were seeded in 96-well culture plate, which was cultured with Dulbecco's modified Eagle medium (DMEM) and 8% fetal bovine serum (FBS) at 37 °C under 5% CO_2 atmosphere for 24 h. Then, 100 µL of DMEM containing the N-doped CDs at a series of concentrations ranging from 50 to 100, 200, 400 and 800 µg mL^{-1} were cultured for another 24 h. Afterwards, 10 µL of 5 mg mL^{-1} of MTT solution was added in to each well and incubated at 37 °C under 5% CO_2 atmosphere for 4 h. Later, the culture medium with MTT was replaced with 100 µL of DMSO. The final mixture was shaken for 10 min at room temperature. The absorbance of MTT at 490 nm was examined by a microplate reader (Thermo Scientific Multiskan GO). The control group was performed without adding N-doped CDs samples. Each experiment was repeated for 4 times.

2.6. *In-vitro* cellular imaging. The cellular fluorescent images were recorded by TCS SP5 laser scanning confocal microscope (CLSM) (Leica, Germany), and a 100$^{\times}$ oil-immersion objective lens (NA=1.40-0.70) was used. 100 µL of HeLa cells (1×10^5 cells mL^{-1}) were cultured in 6-well culture plates, which were cultured with Dulbecco's modified Eagle medium (DMEM) and 8% fetal bovine serum (FBS) at 37 °C under 5% CO_2 atmosphere for 24 h. Later, 200 µg mL^{-1} of N-doped CDs with DMEM medium involving 8% fetal bovine serum (FBS) were added into each well and incubated at 37 °C under 5% CO_2 atmosphere for 24 h. it was followed by removing extra CDs and DMEM medium and washed twice with 1X PBS. The cells were counterstained with 5 µg/mL of DAPI at room temperature in the dark for 5 min. After gentle washing in 10 X PBS for 3 times the cells were fixed on coverslips with 4% freshly prepared paraformaldehyde and sealed with mounting medium for confocal bioimaging.

2.7. *In-vivo* fluorescence imaging. The *in-vivo* fluorescence imaging of mice treated with CDs was carried out using the Xenogen - IVIS® Lumina II imaging system. The athymic BALB/c-nu mice were used with weights 20–25 g. The feasibility of *in-vivo* fluorescence imaging was investigated by sub-

cutaneously (SC) injection of the CDs (50 µL of 0.05, 0.5, and 5 mg CDs in PBS solution, pH 7.4: **CD-EDA$_{(2/1)}$**, **CD-DETA$_{(2/1)}$** and **CD-TEPA$_{(2/1)}$**) into the right side, left side of lower back and right anterior dorsal of three female nude mice. The fluorescence imaging of the mice were obtained at 5 min after injection, with excitation (λ_{ex}) and emission (λ_{em}) wavelengths at λ_{ex}: 535 nm & λ_{em}: 695–770 nm.

3. RESULTS AND DISCUSSION

Three types of N-doped CDs (**CD-EDA**, **CD-DETA** and **CD-TEPA**) were successfully synthesized by hydrothermal carbonization of CA with EDA, DETA and TEPA respectively, at 200 ºC in DDI water solvent for 6 h. To investigate the relationship between the various types of N-doped CDs at different doping amount, we have chosen a series of molar ratios that are based on the number of $–NH_2$ and –COOH groups in reactants with increasing amount of PEA molecule but a fixed amount of CA (details of reaction conditions are shown in Table S3). In order to facilitate morphology variation analysis, we examined each type of CDs that prepared from two different reagents' ratios (RR), *i.e.*, PEA/CA = 2/3, and 2/1 as typical examples.

3.1. The morphology of N-doped CDs. The morphology of three kinds of N-doped CDs, including their size, height and crystallinity, are summarized in Table S1. In fact, these as-prepared CDs were small and with similar contrast to the carbon support film on TEM grid, hence could be hardly observed as clear TEM images. Figure 1 illustrated a notable morphological difference for each type of CDs with increasing RR (PEA/CA); the particles became more difficult to observe when the RR was increased from 2/3 to 2/1. This is possibly due to the higher content of doping agents that excessively reacted with CA, thus less likely to form the shape of particles, but instead formed polymer clusters.[23]

At lower RR (2/3), only **CD-EDA$_{(2/3)}$** showed obvious polycluster-like aggregations. It is interesting that **CD-DETA$_{(2/3)}$** and **CD-TEPA$_{(2/3)}$** are relatively monodispersed and have a quasispherical solid carbon core. In addition, the **CD-EDA$_{(2/1)}$** and **CD-DETA$_{(2/3)}$** showed similar morphologies and had a slight tendency of aggregation. Particle size analyses were performed and fitted by Gaussian distribution (Figure 1, right insets). Most of these CDs have an average size of sub-5 nm. That is, (a) **CD-EDA$_{(2/3)}$** 3.9 ± 0.9 nm, (b) **CD-EDA$_{(2/1)}$** 4.7 ± 0.7 nm, (c) **CD-DETA$_{(2/3)}$** 3.7 ± 1.0 nm, (d) **CD-DETA$_{(2/1)}$** 4.6 ± 0.6 nm, (e) **CD-TEPA$_{(2/3)}$** 4.1 ± 1.4 nm, and (f) **CD-TEPA$_{(2/1)}$** 5.2 ± 1.2 nm. The corresponding elemental composition from XEDS (Figure 1, left insets) showed that CDs mainly consisted of carbon, nitrogen and oxygen. AFM was additionally assisted to illustrate the difference of topographic morphologies among the **CD-EDA$_{(2/3)}$**, **CD-DETA$_{(2/3)}$**, and **CD-TEPA$_{(2/3)}$** (Figure S1). The panels show that **CD-EDA$_{(2/3)}$** appears as bulked nano pieces on mica substrate with average height of 3.24±0.55 nm, which is similar to the morphology of the corresponding TEM images. AFM images of **CD-DETA$_{(2/3)}$** and **CD-TEPA$_{(2/3)}$** show the dispersed particles on mica substrate, whereas the height analyses are 3.20±0.46 nm and 3.52±0.95 nm, respectively. It is

worth noting that AFM images of **CD-EDA$_{(2/1)}$**, **CD-DETA$_{(2/1)}$**, and **CD-TEPA$_{(2/1)}$** are absent here, this is partly due to the inevitable hygroscopic nature of the products with simultaneously induced aggregations during the sample preparations, even at low concentrations. This result suggests that higher amount of doping agents can cause hygroscopically induced aggregation. In order to study the crystallinity of solid phase CDs, XRD investigations was performed. As shown in Figure S2, XRD characterized that all kinds of CDs show a broad diffraction peak centered at $2\theta \approx 20^{\circ}$, implying the amorphous nature of CDs, which are consisting of disordered carbons core with an amorphous surface structure.[24]

3.2. The influence of PEA molecules on formation and component structural features. To further investigate their chemical characteristic relationships, FTIR spectra were applied to determine the organic bonding structures of CDs. In the FTIR spectra of **CD-EDA$_{(2/1)}$**, **CD-DETA$_{(2/1)}$** and **CD-TEPA$_{(2/1)}$** (Figure S3 a, b & c), the typical absorption bands of O–H and N–H stretching vibrations are shown at 3200-3700 cm^{-1} and 3100-3500 cm^{-1}, respectively.[25,26] Also, the amide groups are clearly attributed to C═O stretching vibrations at 1640-1690 cm^{-1} and N–H bending vibrations at 1550-1640 cm^{-1}.[10] These peaks suggest that hydroxyl and amide groups are the main passivating groups on surface molecules of CDs.[27] The absorption peaks at 1350-1480 cm^{-1} and 2850-3000 cm^{-1} are assigned to bending and stretching vibrations of C–H respectively,[9] ascribed to the saturated hydrocarbon joined into the carbon matrix. Moreover, the absorption bands within a range of 1080-1360 cm^{-1} have confirmed the stretching vibrations of C–N group in amine.[26] Further investigations of FTIR on **CD-EDA**, **CD-DETA** and **CD-TEPA** series (Figure S3 b, d & f) have verified the present of amide bond and secondary amines in these N-doped CDs when certain amount of PEA molecules were introduced (for details see the Supporting Information). The Raman spectra further demonstrate the chemical structures of **CD-EDA$_{(2/1)}$**, **CD-DETA$_{(2/1)}$**, and **CD-TEPA$_{(2/1)}$** (Figure S4). Three obvious peaks centered at 1310, 1369 and 1460 cm^{-1} are corresponded to the secondary amines, n-alkane (D band, sp^3-hybridized) and furfurylidene / furoyl groups (aromatic rings), respectively.[28,29] There are certainly no clear G band observed from spectra.

The chemical composition and surface state of CDs at selected doping amounts were examined by the X-ray photoelectron spectroscopy (XPS). The left column of Figure S5 shows the XPS spectra of CDs at low energy resolution, verifying that they consist of mainly carbon, oxygen and nitrogen. Each CD has three peaks centered at 285.5, 399.5 and 532.0 eV, which are corresponded to C1s, N1s and O1s, respectively. The component's ratio analyses for each type of CDs (Table S2) demonstrate that 64.2-71.4% of carbon, 9.8-17% of nitrogen and 14.9-18.7% of oxygen are consisted in CDs, this result reveals that three types of CDs are carbon-rich, O, N-doped and completed through an adequate carbonization.[30] The oxidation levels of oxygen-containing groups, involving hydroxyl (–OH), carboxyl (–COOH) and carbonyl (–C═O) were

investigated via the PL QY against O/C ratio for three kinds of CDs at different doping amounts (Figure 2a). Notably, the O/C ratio of N-doped CDs is not simply correlated with PL QY. In another words, higher PL QY is not always associated with increased oxidation state. For instance, the increased O/C ratio of CD-TEPA accompanied with the reducing of PL QY. In addition, N-doping percentage for each kind of CDs in Table S2, shows comparable doping degrees and no correlation to PL QY. This result suggests that neither the oxidation state nor the N content but the molecule state in CDs plays the key role for enhanced PL performance.

High-resolution XPS (HR-XPS) was applied to give further insight into the molecule state and bonding manner of those elements in N-doped CDs (Figure S5). The C1s and N1s HR-XPS spectra were fitted into Gaussian peaks at 284.5 (C═C/C–C), 286 (C-OH), and 287.5 (C═O) eV for C1s; 399.5 (C═N) and 400.5 (N–C═O) and eV for N1s.[31] it reveals that the presence of sp^2 carbon (C═C/C–C) is associated with the carbonic core in CDs, where the appearance of C–OH, C═O, C═N and N-C═O are corresponded to the oxygen-containing and N-doping groups dominated on surface of the CDs. Interestingly, an increase in intensity of the peak at 286 (C–OH) eV and a decrease in intensity of peak at 287.5 (C═O) eV have accompanied with the elevated amount of nitrogen doping agents in CDs formation (Figure 2 b & c). These features can be interpreted as the enhancement of N-doped CDs water solubility, and the appearance of hygroscopic effect due to the hydrogen bonds between hydroxyl groups and water molecules when the amount of nitrogen doping agents is increased. Furthermore, the peak intensities of C═N at 399.5 eV is correspondingly correlated to PL QY of the CDs. Figure 2 d shows the **CD-EDA$_{(2/1)}$** (10.56%), **CD-DETA$_{(2/1)}$** (10.83%) and **CD-TEPA$_{(1/1)}$** (12.59%) achieved their highest PL QY at 69.3%, 68% and 33.4% respectively. These results imply the increasingly presented of cyclic imines with enhancement of conjugated systems in CDs imparts a superior PL efficiency.[32] We speculated that the high PL QYs of CDs is likely contributed from organic fluorophores, which were connected on the surface or interior of the carbon backbone and can partially contribute to the PL emission.[23] Furthermore, the results from zeta potential measurements found that **CD-EDA$_{(2/1)}$**, **CD-DETA$_{(2/1)}$** and **CD-TEPA$_{(2/1)}$** exhibit negatively charges on particles surface, also proves the appearance of carboxyl groups on surface state of CDs (Figure S6). According to the above results, we proposed a possible formation pathway of N-doped CDs (Scheme 1). Due to the intricate and diverse intermediates formations in harsh reaction condition, no detailed mechanism were provided. Typically, nitrogen doping agents: EDA, DETA and TEPA respectively reacted with CA under the hydrothermal conditions. After the intermolecular and intramolecular dehydration and polymerization among the –COOH, –OH and $–NH_2$ groups, the activated intermediates were carbonized to form the aromatic carbonic rings. N atoms were simultaneously incorporated as pyridinyl, pyrrolyl and amide moieties into the heterocyclic ring systems, and such

precursors were further condensed to form the final CDs.[9,33]

3.3. Structure Effects on Photoluminescence. The UV-Vis absorption and PL spectra of **CD-EDA$_{(2/1)}$**, **CD-DETA$_{(2/1)}$** and **CD-TEPA$_{(2/1)}$** in water solution are quantified and depicted in 3D-Measurements (Figure 3). Emission spectra were acquired at different excitation wavelengths (λ_{ex}) with 10 nm increments from 200 to 450 nm. Two clear absorption bands can be clearly found **CD-EDA$_{(2/1)}$**, **CD-DETA$_{(2/1)}$** and **CD-TEPA$_{(2/1)}$**: a local maximum at 238 nm (P 1) due to π-π* transition of C=C/C=N bonds, and a shoulder band at 350 nm (P 2) associated to the surface passivation state of CDs (illustrated in Figure 3 and Figure S7).[34] The PL emission peaks are located at ca. 445 nm with the λ_{ex} at 238 and 350 nm. Also, the spectra in Figure 3 reveals that the change of λ_{em} intensity is consistent with the corresponding UV-Vis absorption, and excitation-independent PL behavior is found within the λ_{ex} range between 200 and 410 nm (Figure S7). The results suggests that both the size and the surface state of each of these CDs are uniform.[35] Besides, the PL lifetimes (τ) of **CD-EDA$_{(2/1)}$**, **CD-DETA$_{(2/1)}$**, and **CD-TEPA$_{(2/1)}$** are 14, 13 and 10 ns, respectively (Figure. S8). The single exponential decays implied that the source of PL is one single species. In addition, each kind of CDs shows a strong blue, green and extend to far-red PL color (390-600 nm).[13,36,37] Such wide PL bandwidth of CDs may results from the inhomogeneous chemical structure and miscellaneous PL centers. It is worth noting that presence of electron donating groups such as –OH, –NH_2, –NHR, etc.) in a PL centers induces an increase in the molar absorption coefficient and a shift in both absorption and fluorescence spectra through the auxochromic effect.[38] In some conditions for example, the presence of lone pairs of electrons on the oxygen and nitrogen atoms increase the electron density in the π-system, which typically caused by positive mesomeric (+M) effect,[39] as they lower the excited π∗-level, hence a longer wavelength is required for the excitation along π→π∗. Therefore, nitrogen doping and surface passivation could be beneficial to the formation of a conjugated π electron system which may be responsible for the broadband and red-shift emission in the nitrogen doped carbon dots. To further exploring photoluminescence features of the CDs, The UV-Vis absorption properties and the PL QY was investigated for series of N-doped CDs (Figure S9 & S10). It is suggesting that PL QY of the three types of the CDs can be optimized at certain RR ratios, where **CD-EDA$_{(2/1)}$**, **CD-DETA$_{(2/1)}$** and **CD-TEPA$_{(1/1)}$** show the highest PL QY at 69.3%, 68.0% and 33.4%, respectively (Figure 3 d). The PL QY of **CD-EDA** increases with introducing more EDA molecules, it reaches the peak value at ratio of 2/1 (EDA/CA), and then steadily decreases when excessive PEA molecules were participated. Such phenomenon implies that molecule state density can be tuned by altering RR ratio. In order to investigate the structure effect on PL QY, we observed the correlations between UV absorption peak intensity ratios (carbonic core PI 1/ surface state PI 2) and PL QY of each kind of CDs (Figure S11) (for details see the Supporting Information).

The PL stabilities of **CD-EDA$_{(2/1)}$**, **CD-DETA$_{(2/1)}$** and **CD-TEPA$_{(2/1)}$** in water solution were studied via UV illumination for different durations (Figure 4). The results show that **CD-EDA$_{(2/1)}$** and **CD-DETA$_{(2/1)}$** experienced an exponential decay with duration of UV irradiation and suffered a notable PL degradation for more than 160-min exposure, decreasing by more than 50% after a prolonged illumination for 40 and 80 minutes, respectively. However, **CD-TEPA$_{(2/1)}$** shows excellent PL stability in the same period of time, less than 1% loss of PL intensity for 160-min UV exposure. This is noted that the N-doped CDs with higher PL QY may suffered more severe PL degradation under the excitation light, and such phenomenon implies that the photobleaching behavior of **CD-EDA$_{(2/1)}$** and **CD-DETA$_{(2/1)}$** is similar with organic fluorophores. In this regard, the longer chain of PEA molecule gives the better photostability, but lower the PL QYs because less PL centers are formed in CDs.[40,41]

3.4. *In-vitro* cytotoxicity and cellular imaging of CD-EDA$_{(2/1)}$, CD-DETA$_{(2/1)}$ and CD-TEPA$_{(2/1)}$. Cytotoxicity is always one of the important concerns of PL nanomaterials for optical cellular imaging. Hence, to evaluate the toxicity of CDs to cells, HeLa cells were fellow out via the MTT viability assay. HeLa cells were incubated with a series concentration of **CD-EDA$_{(2/1)}$**, **CD-DETA$_{(2/1)}$** and **CD-TEPA$_{(2/1)}$** for 24 h. Figure 5 shows no dramatic change of cell viability in the CD concentrations ranging from 0 to 800 μg mL^{-1}. After 24 h incubation with **CD-EDA$_{(2/1)}$** and **CD-DETA$_{(2/1)}$** separately at concentration of 50 and 100 μg mL^{-1}, the HeLa cells shown the cell viability over 90%. The results of the cell viability test demonstrate that these CDs did not exert any obvious cytotoxicity as the cell viability was over than 80% even at a relatively high concentration (800 μg mL^{-1}) of CDs. Despite the increases of cytotoxicity with elevated concentration, these CDs have shown a comparable or better biocompatibility to those reported fluorescent GQDs.[42-45]

Based on low toxicity and notable fluorescence performance of these N-doped CDs, the *in-vitro* cellular imaging and cellular uptake were monitored by using laser scanning confocal microscope (CLSM) for cancerous HeLa cells. The fluorescence images of HeLa cells incubated with **CD-EDA$_{(2/1)}$**, **CD-DETA$_{(2/1)}$** and **CD-TEPA$_{(2/1)}$** at concentration of 200 μg mL^{-1} in PBS buffer for 4 h are illustrated in Figure 6 (The excitation wavelength/emission bandpass filters for each type of CDs are indicated on the top of the image). A strong green fluorescence in HeLa cells are displayed using λ_{ex} at 488 nm when incubated with **CD-EDA$_{(2/1)}$** and **CD-DETA$_{(2/1)}$**, green channel shows CDs are evenly distributed in cytoplasm region and some of the CDs can be found in nucleolus but lesser signal observed in nucleus. Meanwhile the red channel (λ_{ex} = 561 nm) shows a weakened fluorescent signal for all kinds of CDs. Furthermore, cells incubated with **CD-DETA$_{(2/1)}$** show a slightly lower brightness than **CD-EDA$_{(2/1)}$** at red channel under the same experimental conditions, but still bright enough to distinguish the cell membrane and the cytoplasm of the HeLa cells. When compared with the former **CD-EDA$_{(2/1)}$** and **CD-DETA$_{(2/1)}$** group, the **CD-TEPA$_{(2/1)}$** image group (Figure 6 bot-

tom row) appeared with relative unsatisfied fluorescent brightness in the cytoplasm of the cells. To further confirm the localization of the CDs inside the cells, we stained the cell nuclei with DAPI (Figure 6 blue channel). We observed that the CDs were preferentially located at the cytoplasm and nucleolus (Figure 6 Overlay) as detected by confocal microscopy. The uptake of these CDs by the HeLa cells could be similar to the pathway for some GQDs,[46-48] which penetrate to the cell membrane by disturbing the structure and conformation of the lipid bilayer.[44,45]

3.5. *In-vivo* fluorescence imaging. The evaluation of N-doped CDs with increased doses for *in-vivo* optical bioimaging was investigated in mice. 50 µL of 0.05, 0.5, and 5 mg CDs (**CD-EDA$_{(2/1)}$**, **CD-DETA$_{(2/1)}$** and **CD-TEPA$_{(2/1)}$**) were injected subcutaneously (SC) into the right side, left side of lower back and right anterior dorsal of nude mice, respectively (blue arrows in Figure 7 ai, bi & ci). The fluorescence imaging of the mice were captured with excitation (λ_{ex}) and emission (λ_{em}) wavelengths at λ_{ex}: 535 nm & λ_{em}: 695–770 nm.

The true color fluorescent composite images (Figure 7 ai, bi & ci) show CDs signals at different injection sites among autofluorescence background (mice skin). Figure 7 aii, bii & cii depict filtered CDs signals and clearly show the whole animal and most of the injection sites. The fluorescent signal of three types of CDs can be readily visualized when 0.5 and 5 mg of CDs were injected, which indicate that these CDs are capable for *in-vivo* optical imaging by using extended excitation wavelength and gaining desirable far-red light signal. Notably, the large Stokes shift provided the CDs with significant benefit for fluorescence bioimaging, because far-red emission wavelength provide a better penetration ability than the visible light for *in-vivo* fluorescence imaging.[49-51] To further investigate the *in-vivo* optical performance of CDs with different doses, the amount of light emission were quantified by using the ROIs tool to measure surface fluorescent intensities in pseudo-color *in-vivo* images (Figure 7 aiii, biii & ciii). As shown in Figure 8, the signal intensity of CDs decreased with reducing doses from 5 mg and 0.5mg to 0.05 mg. It is noticed that 5 mg dose of **CD-EDA$_{(2/1)}$** shows a highest performance with signal intensity above 1×10^5, and slightly drop to 87% with 10-fold-lower dose. Both **CD-DETA$_{(2/1)}$** and **CD-TEPA$_{(2/1)}$** show lower intensities than **CD-EDA$_{(2/1)}$** at corresponding doses. However, the signal intensity of all types CDs decrease to around 3×10^4 when lower dose of 0.05 mg is used. It is indicated that some of the incomplete filtered autofluorescence of mice with intensity near 3×10^4 is significantly disturbing the CDs signal because of their similar emission wavelength. Thereby, such low amount of CDs may not be able to provide enough signal for imaging due to the disturbance from uncertain autofluorescence of mice. Overall, quantitation of in-vivo **CD-EDA$_{(2/1)}$**, **CD-DETA$_{(2/1)}$** and **CD-TEPA$_{(2/1)}$** fluorescence imaging show clear signals for both high dose (5 mg) and low dose (0.5 mg) studies. Imaging results for these CDs correlated well with their corresponding optical performance. In fact, these CDs are relatively small and comparable in size to those fluorescent proteins (≈ 5 nm),[52] the negatively charged CDs which

are known to be less toxic due to their limited interaction with the negatively charged surface of cell membranes compared to nanoparticles with cationic properties,[53-56] Finally, we have demonstrated that the non-labeled N-doped CDs could potentially serve as optical contrast agents to highlight normal tissues (such as nerves) for image-guided surgery are desirable.[57-60]

4. CONCLUSIONS

In summary, we have reported for the first time on enhanced photoluminescence (PL) performance influence by structure effect among the various types of nitrogen atom doped (N-doped) PL CDs that synthesized from the hydrothermal reaction of linear PEA analogues and CA in different ratios. Our result implies that fluorophores appeared as the building blocks in carbonic domains of these CDs, and the hybridization between molecule state and the carbon backbone play an important role in PL mechanism of these CDs; the increasing of amine group in PEA molecules can also govern the molecule state for the CDs formation. We have also demonstrated the feasibility of N-doped CDs for *in-vivo*/*in-vitro* optical bioimaging with desirable photoluminescence signal and good biocompatibility. By taking advantage from their broad emission peaks, high PL QYs and ultracompact size (≈ 5 nm) can be potentially used for *in-vitro* and *in-vivo* bioimaging applications. Such ultracompact N-doped CDs with adjustable surface charge may also useful as 'model CDs,' stimulate further study on helping researchers to understand the *in-vivo* behavior of nano-sized particles with similar size and shape.

ASSOCIATED CONTENT

Supporting Information

AFM, XRD, FTIR, Raman spectra, XPS, Zeta potentials, PL lifetime, UV-Vis absorption, PL QY, additional data and discussion of the analysis.

AUTHOR INFORMATION

Corresponding Authors

*K.C.F.L: Email: cfleung@hkbu.edu.hk. Phone: (852) 3411 2319

*Y.X.W: Email: yixiang_wang@cuhk.edu.hk.

ACKNOWLEDGMENTS

This work was partially supported by General Research Fund (201412 and 201213) from The Hong Kong Research Grants Council. The authors thank Mr. Zhicheng Zhong at Guangdong Women and Children Hospital, China, for his kind helps for parts of the experiment.

REFERENCES

1. Qiao, Z. A.; Wang, Y. F.; Gao, Y.; Li, H. W.; Dai, T. Y.; Liu, Y. L.; Huo, Q. S. Commercially activated carbon as the source for producing multicolor photoluminescent carbon dots by chemical oxidation. *Chem. Commun.* **2010**, *46*, 8812-8814.

2. Shinde, D. B.; Pillai, V. K. Electrochemical Preparation of Luminescent Graphene Quantum Dots from Multiwalled Carbon Nanotubes. *Chem. Eur. J.* **2012**, *18*, 12522-12528.

3. Xu, X. Y.; Ray, R.; Gu, Y. L.; Ploehn, H. J.; Gearheart, L.; Raker, K.; Scrivens, W. A. Electrophoretic analysis and purification of fluorescent single-walled carbon nanotube fragments. *J. Am. Chem. Soc.* **2004**, *126*, 12736-12737.

4. Zhao, Q. L.; Zhang, Z. L.; Huang, B. H.; Peng, J.; Zhang, M.; Pang, D. W. Facile preparation of low cytotoxicity fluorescent carbon nanocrystals by electrooxidation of graphite. *Chem. Commun.* **2008**, *44*, 5116-5118.

5. Sun, Y. P.; Zhou, B.; Lin, Y.; Wang, W.; Fernando, K. A. S.; Pathak, P.; Meziani, M. J.; Harruff, B. A.; Wang, X.; Wang, H. F.; Luo, P. J. G.; Yang, H.; Kose, M. E.; Chen, B. L.; Veca, L. M.; Xie, S. Y. Quantum-sized carbon dots for bright and colorful photoluminescence. *J. Am. Chem. Soc.* **2006**, *128*, 7756-7757.
6. Dong, Y. Q.; Wang, R. X.; Li, H.; Shao, J. W.; Chi, Y. W.; Lin, X. M.; Chen, G. N. Polyamine-functionalized carbon quantum dots for chemical sensing. *Carbon.* **2012**, *50*, 2810-2815.
7. Wu, X.; Tian, F.; Wang, W. X.; Chen, J.; Wu, M.; Zhao, J. X. Fabrication of highly fluorescent graphene quantum dots using L-glutamic acid for in vitro/in vivo imaging and sensing. *J. Mater. Chem. C.* **2013**, *1*, 4676-4684.
8. Zhu, H.; Wang, X. L.; Li, Y. L.; Wang, Z. J.; Yang, F.; Yang, X. R. Microwave synthesis of fluorescent carbon nanoparticles with electrochemiluminescence properties. *Chem. Commun.* **2009**, *45*, 5118-5120.
9. Zhu, S. J.; Meng, Q. N.; Wang, L.; Zhang, J. H.; Song, Y. B.; Jin, H.; Zhang, K.; Sun, H. C.; Wang, H. Y.; Yang, B. Highly Photoluminescent Carbon Dots for Multicolor Patterning, Sensors, and Bioimaging. *Angew. Chem., Int. Ed.* **2013**, *52*, 3953–3957.
10. Qu, D.; Zheng, M.; Zhang, L. G.; Zhao, H. F.; Xie, Z. G.; Jing, X. B.; Haddad, R. E.; Fan, H. Y.; Sun, Z. C. Formation mechanism and optimization of highly luminescent N-doped graphene quantum dots. *Sci. Rep.* **2014**, *4*, 5294.
11. Wei, W. L.; Xu, C.; Wu, L.; Wang, J. S.; Ren, J. S.; Qu, X. G. Non-Enzymatic-Browning-Reaction: A Versatile Route for Production of Nitrogen-Doped Carbon Dots with Tunable Multicolor Luminescent Display. *Sci. Rep.* **2014**, *4*, 3564.
12. Wang, W.; Li, Y. M.; Cheng, L.; Cao, Z. Q.; Liu, W. G. Water-soluble and phosphorus-containing carbon dots with strong green fluorescence for cell labeling. *J. Mater. Chem. B.* **2014**, *2*, 46-48.
13. Bhunia, S. K.; Saha, A.; Maity, A. R.; Ray, S. C.; Jana, N. R. Carbon Nanoparticle-based Fluorescent Bioimaging Probes. *Sci. Rep.* **2013,** *3*, 1473.
14. Chandra, S.; Patra, P.; Pathan, S. H.; Roy, S.; Mitra, S.; Layek, A.; Bhar, R.; Pramanik, P.; Goswami, A. Luminescent S-doped carbon dots: an emergent architecture for multimodal applications. *J. Mater. Chem. B.* **2013**, *1*, 2375-2382.
15. Yan, X.; Cui, X.; Li, L. S. Synthesis of Large, Stable Colloidal Graphene Quantum Dots with Tunable Size. *J. Am. Chem. Soc.* **2010**, *132*, 5944-5945.
16. Pan, D. Y.; Zhang, J. C.; Li, Z.; Wu, M. H. Hydrothermal Route for Cutting Graphene Sheets into Blue-Luminescent Graphene Quantum Dots. *Adv. Mater.* **2010**, *22*, 734-735.
17. Baker, S. N.; Baker, G. A. Luminescent Carbon Nanodots: Emergent Nanolights. *Angew. Chem., Int. Ed.* **2010**, *49*, 6726-6744.
18. Jin, S. H.; Kim, D. H.; Jun, G. H.; Hong, S. H.; Jeon, S. Tuning the Photoluminescence of Graphene Quantum Dots through the Charge Transfer Effect of Functional Groups. *ACS Nano* **2013**, *7*, 1239–1245.
19. Wang, Y. X.; Wang, D. W.; Zhu, X. M.; Zhao, F.; Leung, K. C. Carbon coated superparamagnetic iron oxide nanoparticles for sentinel lymph nodes mapping. *Quant. Imaging. Med. Surg.* **2012**, *2*, 53-56.
20. Williams, A. T. R.; Winfield, S. A.; Miller, J. N. Relative Fluorescence Quantum Yields Using a Computer-Controlled Luminescence Spectrometer. *Analyst.* **1983**, *108*, 1067-1071.
21. Melhuish, W. H. Quantum Efficiencies of Fluorescence of Organic Substances: Effect of Solvent and Concentration of the Fluorescent Solute. *J. Phys. Chem.* **1961**, *65*, 229-235.
22. Dhami, S.; Demello, A. J.; Rumbles, G.; Bishop, S. M.; Phillips, D.; Beeby, A. Phthalocyanine Fluorescence at High-Concentration - Dimers or Reabsorption Effect. *Photochem. Photobiol.* **1995**, *61*, 341-346.
23. Song, Y. B.; Zhu, S. J.; Xiang, S. Y.; Zhao, X. H.; Zhang, J. H.; Zhang, H.; Fu, Y.; Yang, B. Investigation into the fluorescence quenching behaviors and applications of carbon dots. *Nanoscale.* **2014**, *6*, 4676-4682.
24. Liu, S. S.; Wang, C. F.; Li, C. X.; Wang, J.; Mao, L. H.; Chen, S. Hair-derived carbon dots toward versatile multidimensional fluorescent materials. *J. Mater. Chem. C.* **2014**, *2*, 6477-6483.
25. Wang, F.; Pang, S. P.; Wang, L.; Li, Q.; Kreiter, M.; Liu, C. Y. One-Step Synthesis of Highly Luminescent Carbon Dots in Noncoordinating Solvents. *Chem. Mater.* **2010**, *22*, 4528-4530.
26. Zheng, M.; Xie, Z. G.; Qu, D.; Li, D.; Du, P.; Jing, X. B.; Sun, Z. C. On Off On Fluorescent Carbon Dot Nanosensor for Recognition of Chromium(VI) and Ascorbic Acid Based on the Inner Filter Effect. *ACS Appl. Mater. Interfaces.* **2013**, *5*, 13242-13247.
27. Yu, K. H.; Yoo, Y. H.; Rhee, J. M.; Lee, M. H.; Yu, S. C. Two-dimensional Raman correlation spectroscopy study of the pathway for the thermal

imidization of poly(amic acid). *Bull. Korean Chem. Soc.* **2003**, *24*, 357-362.
28. Li, H. T.; Kang, Z. H.; Liu, Y.; Lee, S. T. Carbon nanodots: synthesis, properties and applications. *J. Mater. Chem.* **2012**, *22*, 24230-24253.
29. Parker, F. S. *Applications of infrared, raman, and resonance raman spectroscopy in biochemistry*; Plenum Press: New York, 1983. p xiv, p 550.
30. Zhang, S.; Tsuzuki, S.; Ueno, K.; Dokko, K.; Watanabe, M. Upper Limit of Nitrogen Content in Carbon Materials. *Angew. Chem., Int. Ed.* **2015**, *54*, 1302-1306.
31. Tang, L. B.; Ji, R. B.; Li, X. M.; Bai, G. X.; Liu, C. P.; Hao, J. H.; Lin, J. Y.; Jiang, H. X.; Teng, K. S.; Yang, Z. B.; Lau, S. P. Deep Ultraviolet to Near-Infrared Emission and Photoresponse in Layered N-Doped Graphene Quantum Dots. *ACS Nano* **2014**, *8*, 6312-6320.
32. Wang, Q.; Lee, S. F.; Tang, C. Y.; Yu, J. C. M.; Leung, K. C. F.; Wong, K. W. Azobenzene dendronized carbon nanoparticles: the effect of light antenna. *RSC Adv.* **2014**, *4*, 18193-18197.
33. Chen, X. X.; Jin, Q. Q.; Wu, L. Z.; Tung, C. H.; Tang, X. J. Synthesis and Unique Photoluminescence Properties of Nitrogen-Rich Quantum Dots and Their Applications. *Angew. Chem., Int. Ed.* **2014**, *53*, 12542-12547.
34. Wang, Y.; Kalytchuk, S.; Zhang, Y.; Shi, H. C.; Kershaw, S. V.; Rogach, A. L. Thickness-Dependent Full-Color Emission Tunability in a Flexible Carbon Dot Ionogel. *J. Phys. Chem. Lett.* **2014**, *5*, 1412-1420.
35. Dong, Y. Q.; Shao, J. W.; Chen, C. Q.; Li, H.; Wang, R. X.; Chi, Y. W.; Lin, X. M.; Chen, G. N. Blue luminescent graphene quantum dots and graphene oxide prepared by tuning the carbonization degree of citric acid. *Carbon.* **2012**, *50*, 4738-4743.
36. Li, H. T.; He, X. D.; Kang, Z. H.; Huang, H.; Liu, Y.; Liu, J. L.; Lian, S. Y.; Tsang, C. H. A.; Yang, X. B.; Lee, S. T. Water-Soluble Fluorescent Carbon Quantum Dots and Photocatalyst Design. *Angew. Chem., Int. Ed.* **2010**, *49*, 4430-4434.
37. Liu, H. P.; Ye, T.; Mao, C. D. Fluorescent carbon nanoparticles derived from candle soot. *Angew. Chem., Int. Ed.* **2007**, *46*, 6473-6475.
38. Valeur, B.; Berberan-Santos, M. N. Structural Effects on Fluorescence Emission. In *Molecular Fluorescence Priciples and Applications*, Wiley-VCH, 2012, p.77.
39. Basheer, M. C., Santhosh, U.; Alex, S.; Thomas, K. G.; Suresh, C. H.; Das, S. Design and synthesis of squaraine based near infrared fluorescent probes. *Tetrahedron* **2007**, *63*, 1617-1623.
40. Wang, L.; Zhu, S. J.; Wang, H. Y.; Qu, S. N.; Zhang, Y. L.; Zhang, J. H.; Chen, Q. D.; Xu, H. L.; Han, W.; Yang, B.; Sun, H. B. Common Origin of Green Luminescence in Carbon Nanodots and Graphene Quantum Dots. *ACS Nano* **2014**, *8*, 2541-2547.
41. Zhu, S.; Song, Y.; Zhao, X.; Shao, J.; Zhang, J.; Yang, B. The photoluminescence mechanism in carbon dots (graphene quantum dots, carbon nanodots, and polymer dots): current state and future perspective. *Nano. Res.* **2015**, *8*, 355-381.
42. Chong, Y.; Ma, Y. F.; Shen, H.; Tu, X. L.; Zhou, X.; Xu, J. Y.; Dai, J. W.; Fan, S. J.; Zhang, Z. J. The in vitro and in vivo toxicity of graphene quantum dots. *Biomaterials.* **2014**, *35*, 5041-5048.
43. Nurunnabi, M.; Khatun, Z.; Huh, K. M.; Park, S. Y.; Lee, D. Y.; Cho, K. J.; Lee, Y. K. In Vivo Biodistribution and Toxicology of Carboxylated Graphene Quantum Dots. *ACS Nano* **2013**, *7*, 6858-6867.
44. Wang, T.; Zhu, S.; Jiang, X. Toxicity mechanism of graphene oxide and nitrogen-doped graphene quantum dots in RBCs revealed by surface-enhanced infrared absorption spectroscopy. *Toxicology. Research.* **2015**, *4*, 885-894.
45. Yuan, X. C.; Liu, Z. M.; Guo, Z. Y.; Ji, Y. H.; Jin, M.; Wang, X. P. Cellular distribution and cytotoxicity of graphene quantum dots with different functional groups. *Nanoscale Res. Lett.* **2014**, *9*, 1-9.
46. Roy, P.; Periasamy, A. P.; Lin, C.-Y.; Her, G.-M.; Chiu, W.-J.; Li, C.-L.; Shu, C.-L.; Huang, C.-C.; Liang, C.-T.; Chang, H.-T. Photoluminescent graphene quantum dots for in vivo imaging of apoptotic cells. *Nanoscale.* **2015**, *7*, 2504-2510.
47. Sahu, S.; Behera, B.; Maiti, T. K.; Mohapatra, S. Simple one-step synthesis of highly luminescent carbon dots from orange juice: application as excellent bio-imaging agents. *Chem. Commun.* **2012**, *48*, 8835-8837.
48. Zhang, M.; Bai, L. L.; Shang, W. H.; Xie, W. J.; Ma, H.; Fu, Y. Y.; Fang, D. C.; Sun, H.; Fan, L. Z.; Han, M.; Liu, C. M.; Yang, S. H. Facile synthesis of water-soluble, highly fluorescent graphene quantum dots as a robust biological label for stem cells. *J. Mater. Chem.* **2012**, *22*, 7461-7467.
49. Lee, J. H.; Park, G.; Hong, G. H.; Choi, J.; Choi, H. S. Design considerations for targeted optical contrast agents. *Quant. Imaging. Med. Surg.* **2012**, *2*, 266-273.

50. Park, K. Polysaccharide-based near-infrared fluorescence nanoprobes for cancer diagnosis. *Quant. Imaging. Med. Surg.* **2012**, *2*, 106-113.
51. Wang, Y. G.; Kim, H.; Mun, S.; Kim, D.; Choi, Y. Indocyanine green-loaded perfluorocarbon nanoemulsions for bimodal (19)F-magnetic resonance/nearinfrared fluorescence imaging and subsequent phototherapy. *Quant. Imaging. Med. Surg.* **2013**, *3*, 132-140.
52. LeCroy, G. E.; Sonkar, S. K.; Yang, F.; Veca, L. M.; Wang, P.; Tackett, K. N.; Yu, J. J.; Vasile, E.; Qian, H. J.; Liu, Y. M.; Luo, P.; Sun, Y. P. Toward Structurally Defined Carbon Dots as Ultracompact Fluorescent Probes. *ACS Nano* **2014**, *8*, 4522-4529.
53. Knudsen, K. B.; Northeved, H.; Kumar, E. K. P.; Permin, A.; Andresen, T. L.; Larsen, S.; Wegener, K. M.; Lam, H. R.; Lykkesfeldt, J. Differential toxicological response to positively and negatively charged nanoparticles in the rat brain. *Nanotoxicology.* **2014**, *8*, 764-774.
54. Nakanishi, T.; Kunisawa, J.; Hayashi, A.; Tsutsumi, Y.; Kubo, K.; Nakagawa, S.; Fujiwara, H.; Hamaoka, T.; Mayumi, T. Positively charged liposome functions as an efficient immunoadjuvant in inducing immune responses to soluble proteins. *Biochem. Biophys. Res. Commun.* **1997**, *240*, 793-797.
55. Nakanishi, T.; Kunisawa, J.; Hayashi, A.; Tsutsumi, Y.; Kubo, K.; Nakagawa, S.; Nakanishi, M.; Tanaka, K.; Mayumi, T. Positively charged liposome functions as an efficient immunoadjuvant in inducing cell-mediated immune response to soluble proteins. *J. Control. Release.* **1999**, *61*, 233-240.
56. Soenen, S. J. H.; Brisson, A. R.; De Cuyper, M. Addressing the problem of cationic lipid-mediated toxicity: The magnetoliposome model. *Biomaterials.* **2009**, *30*, 3691-3701.
57. Gibbs, S. L. Near infrared fluorescence for image-guided surgery. *Quant. Imaging. Med. Surg.* **2012**, *2*, 177-187.
58. Idee, J. M.; Louguet, S.; Ballet, S.; Corot, C. Theranostics and contrast-agents for medical imaging: a pharmaceutical company viewpoint. *Quant. Imaging. Med. Surg.* **2013**, *3*, 292-297.
59. Tung, C. H. Colorful lighting in the operating room. *Quant. Imaging. Med. Surg.* **2013**, *3*, 186-188.
60. Wang, Y. X.; Ng, C. K. The impact of quantitative imaging in medicine and surgery: Charting our course for the future. *Quant. Imaging. Med. Surg.* **2011**, *1*, 1-3.

Figures

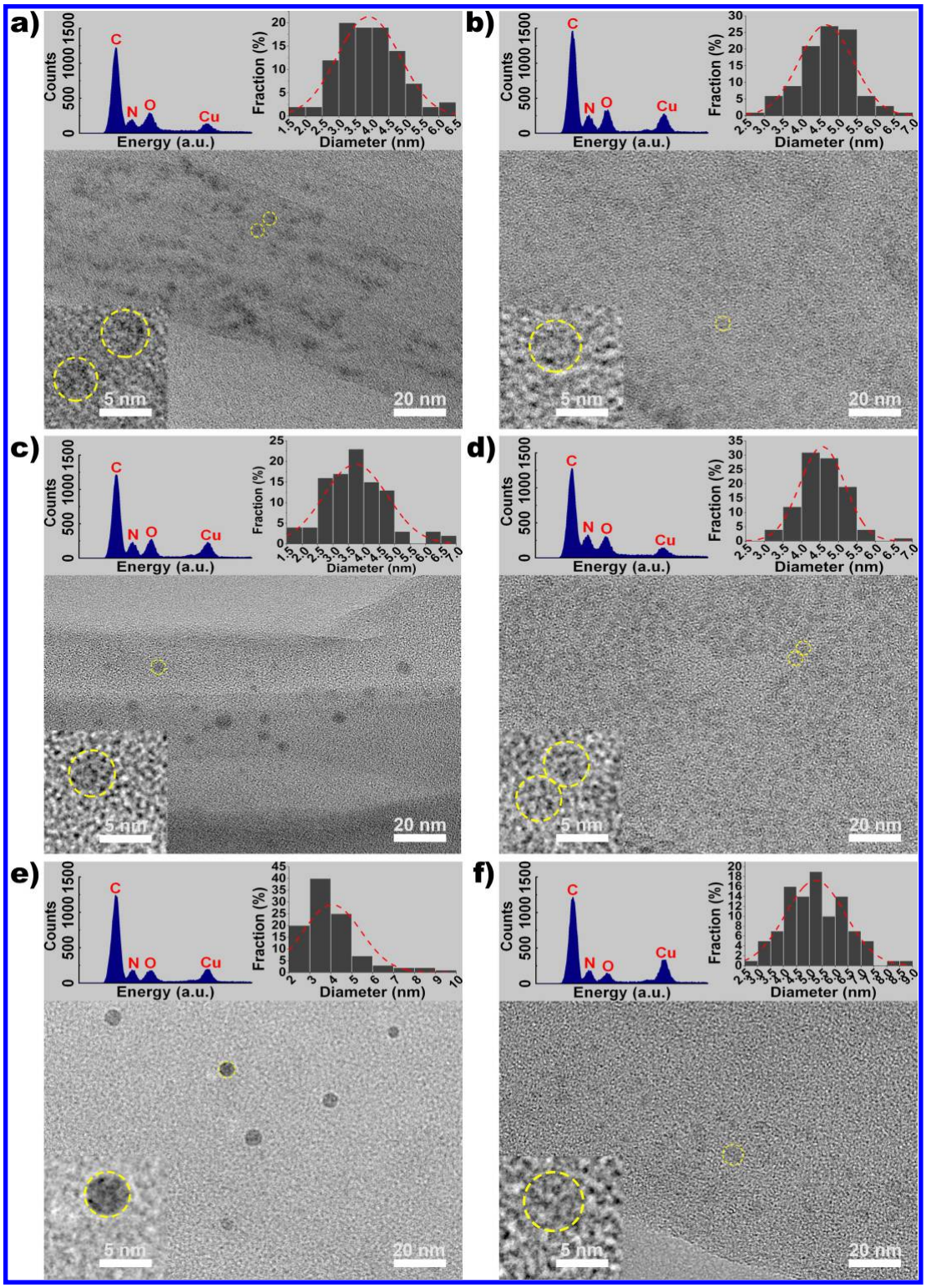

Figure 1. Representative TEM images of N-doped CDs with different ratios of base (EDA, DETA or TEPA) and citric acid (CA). (a) EDA/CA 2/3 (**CD-EDA$_{(2/3)}$**), (b) EDA/CA 2/1 (**CD-EDA$_{(2/1)}$**), (c) DETA/CA 2/3 (**CD-DETA$_{(2/3)}$**), (d) DETA/CA 2/1 (**CD-DETA$_{(2/1)}$**), (e) TEPA/CA 2/3 (**CD-TEPA$_{(2/3)}$**), and (f) TEPA/CA 2/1 (**CD-TEPA$_{(2/1)}$**). Scale bar = 20 nm. The corresponding XEDS for elemental analysis, particle size distribution and HRTEM images (scale bar 5 nm) are shown as top left, top right and bottom left insets, respectively.

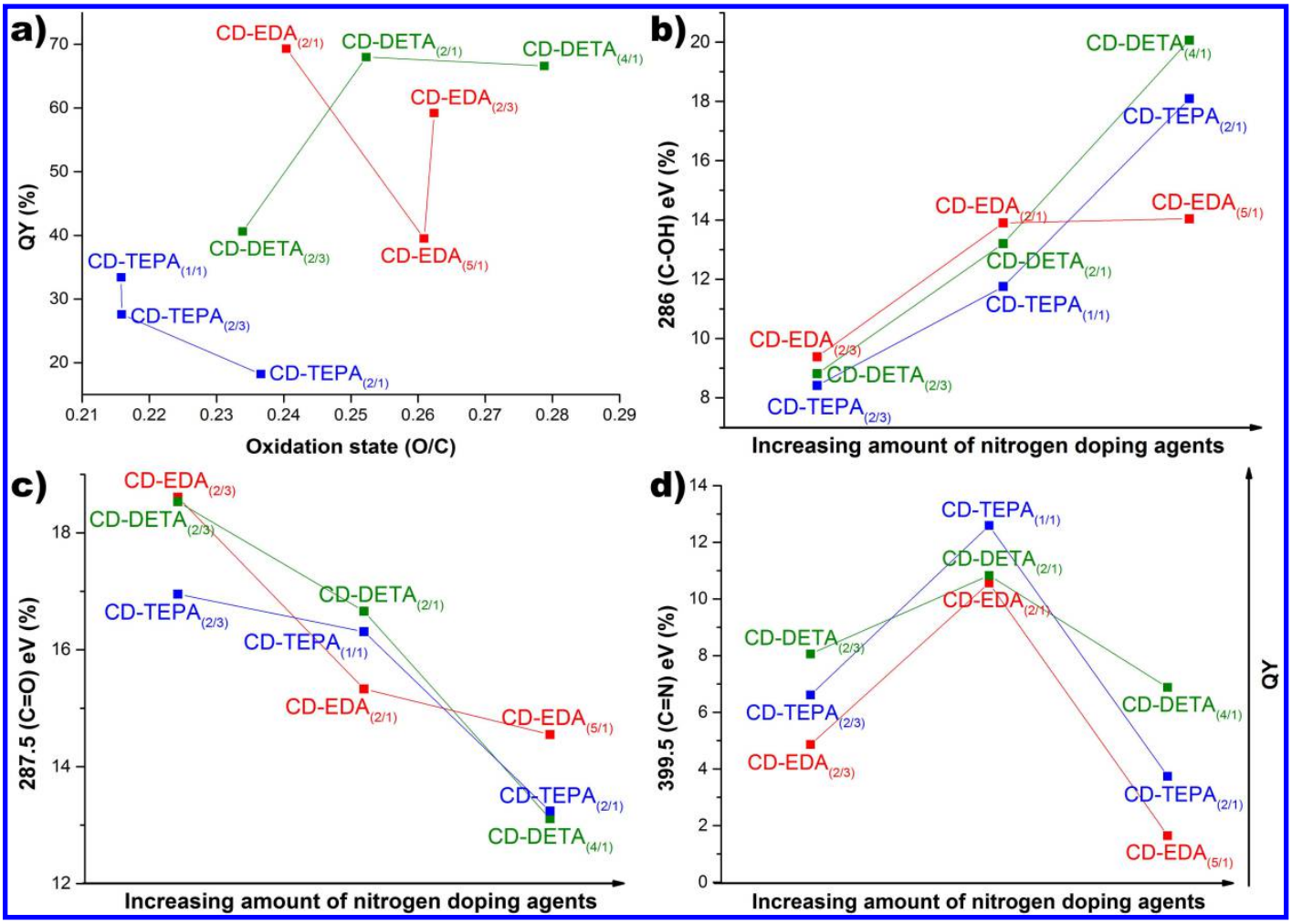

Figure 2. a) QY against O/C ratio of CDs. Peak intensity of b) C–OH (ca. 286 eV), c) C═O (ca. 287.5 eV), and d) C═N (ca. 399.5 eV) vs. the amount of N-doping agents participated in CDs formation.

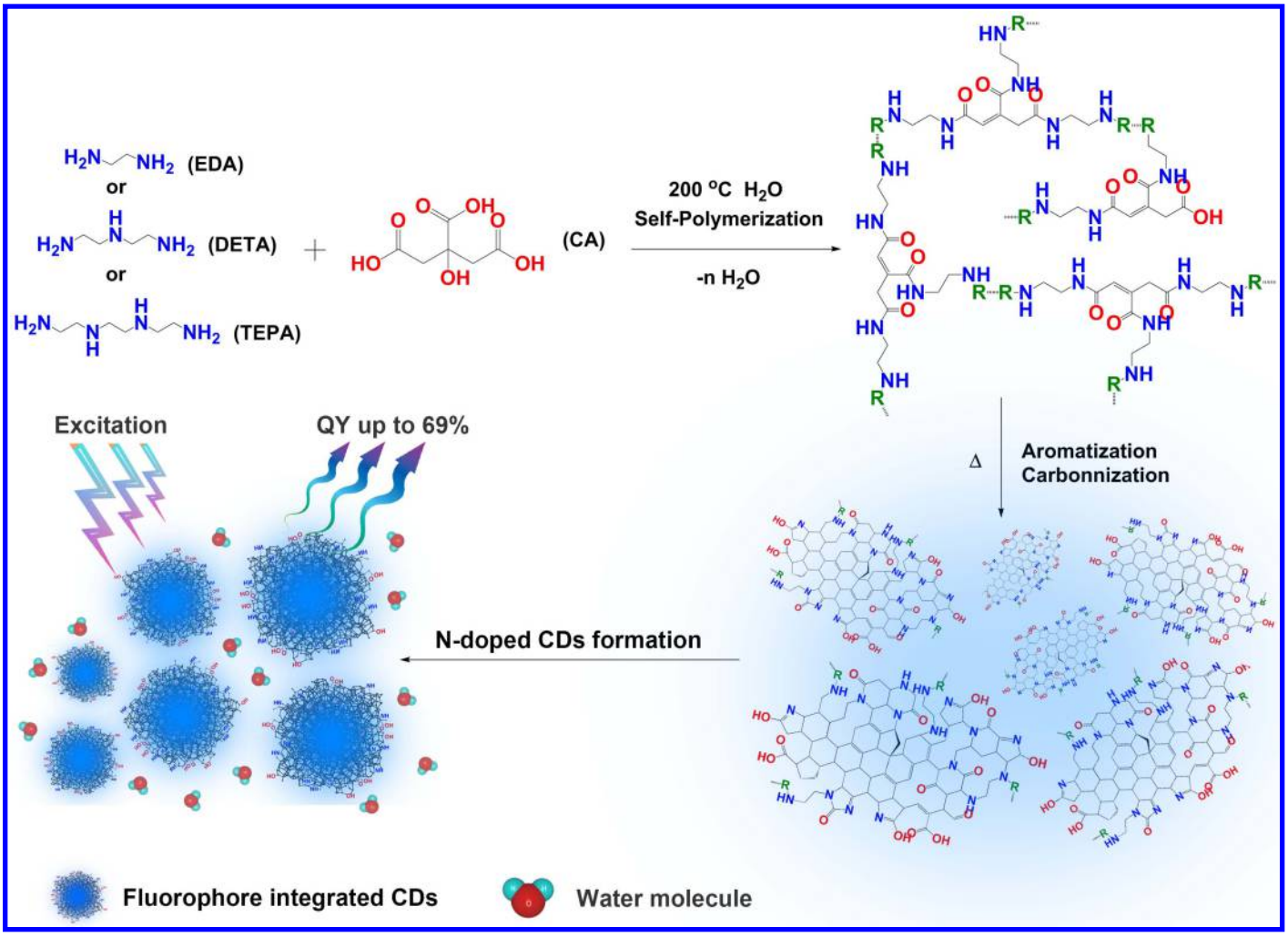

Scheme 1. Proposed formation pathway of N-doped CDs.

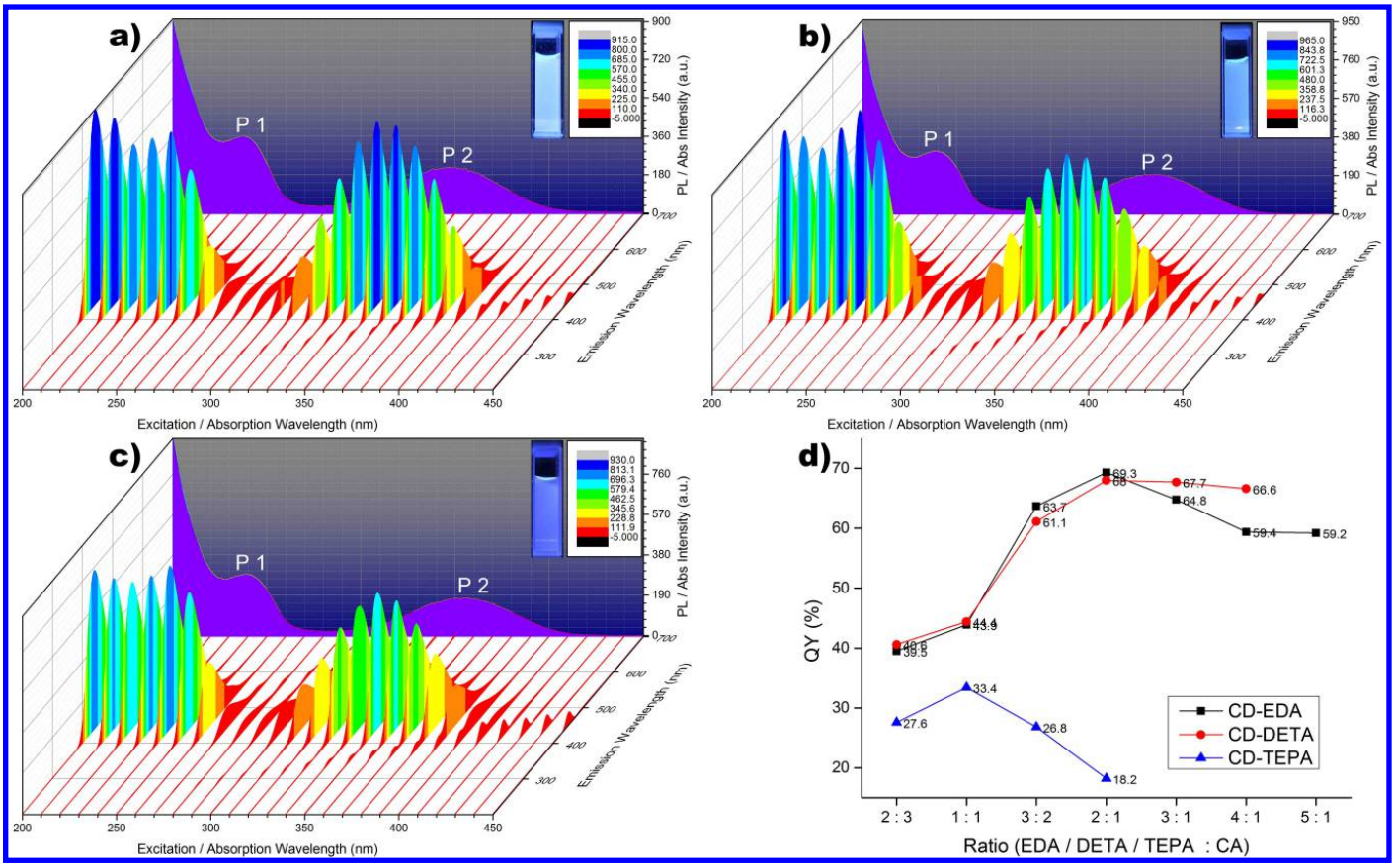

Figure 3. 3D PL spectra under the excitation wavelengths range from 200-450 nm with 10 nm increments (colored) and UV-Vis absorption spectra of N-doped CDs (purple). a) **CD-EDA$_{(2/1)}$**, b) **CD-DETA$_{(2/1)}$**, c) **CD-TEPA$_{(2/1)}$**. d) The PL QYs of three kinds of CDs prepared from increasing amount of N-doping agents. (a, b, c, right inserts) The blue fluorescent lights of three CDs observed under the UV illumination at 365 nm.

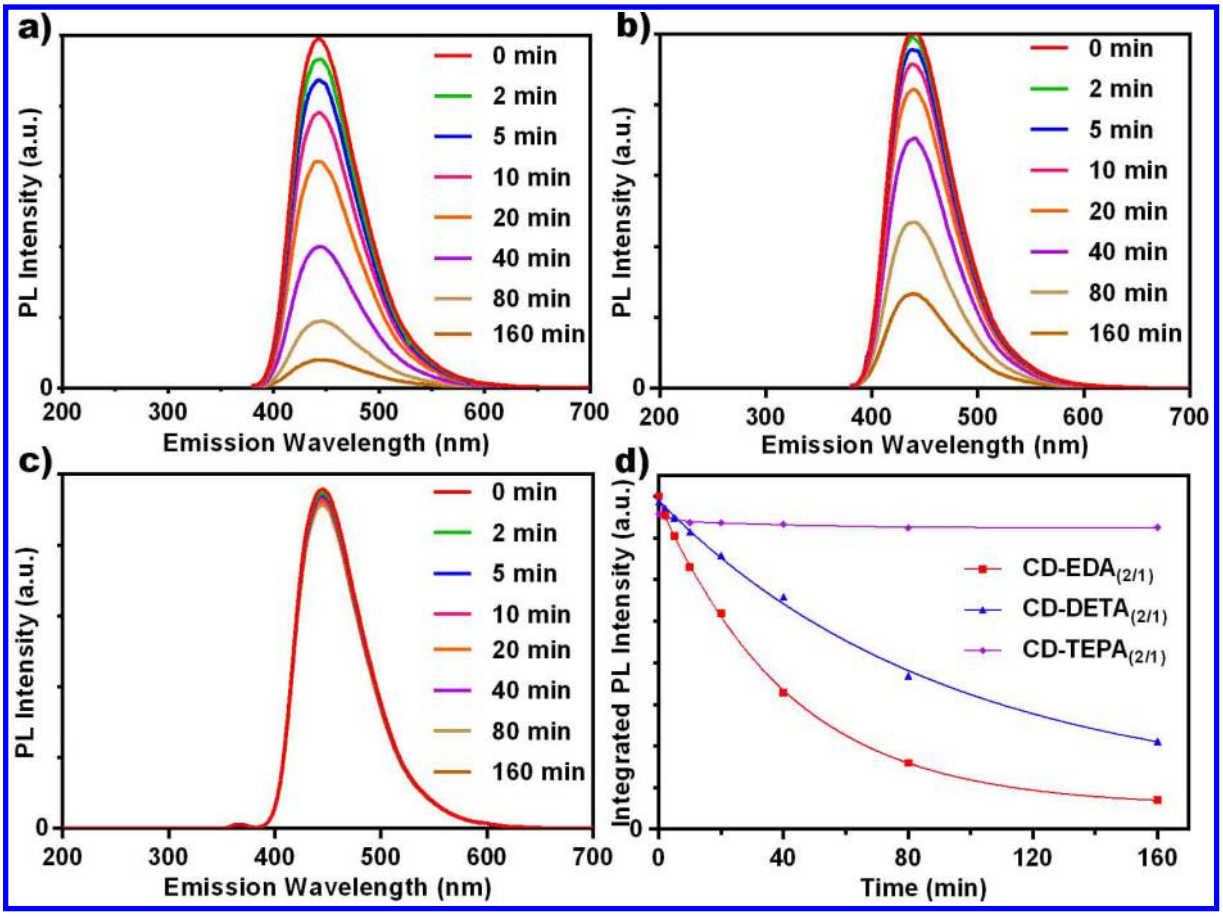

Figure 4. PL intensity of (a) **CD-EDA$_{(2/1)}$**, (b) **CD-DETA$_{(2/1)}$** and (c) **CD-TEPA$_{(2/1)}$** to the continued UV illumination for 0, 2, 5, 10, 20, 40, 80, and 160 minutes. (d) The photostability of these three CDs illustrated by the exponential decay curves of their PL intensities.

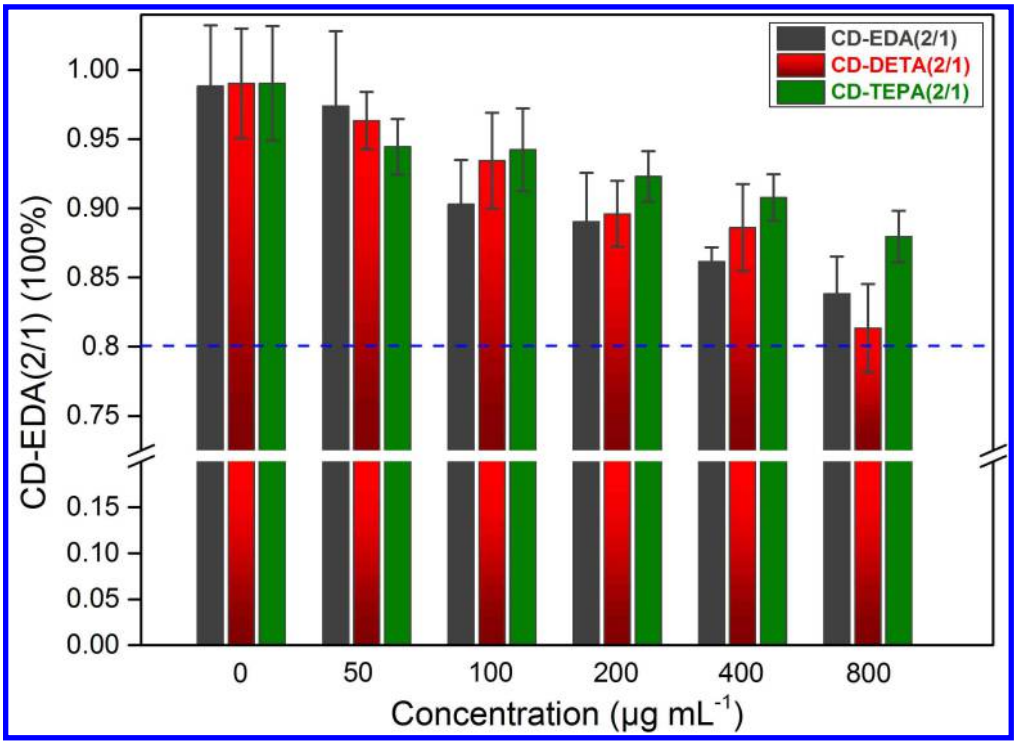

Figure 5. *In-vitro* cytotoxicity testing results of CDs with various concentrations against HeLa cells from an MTT assay.

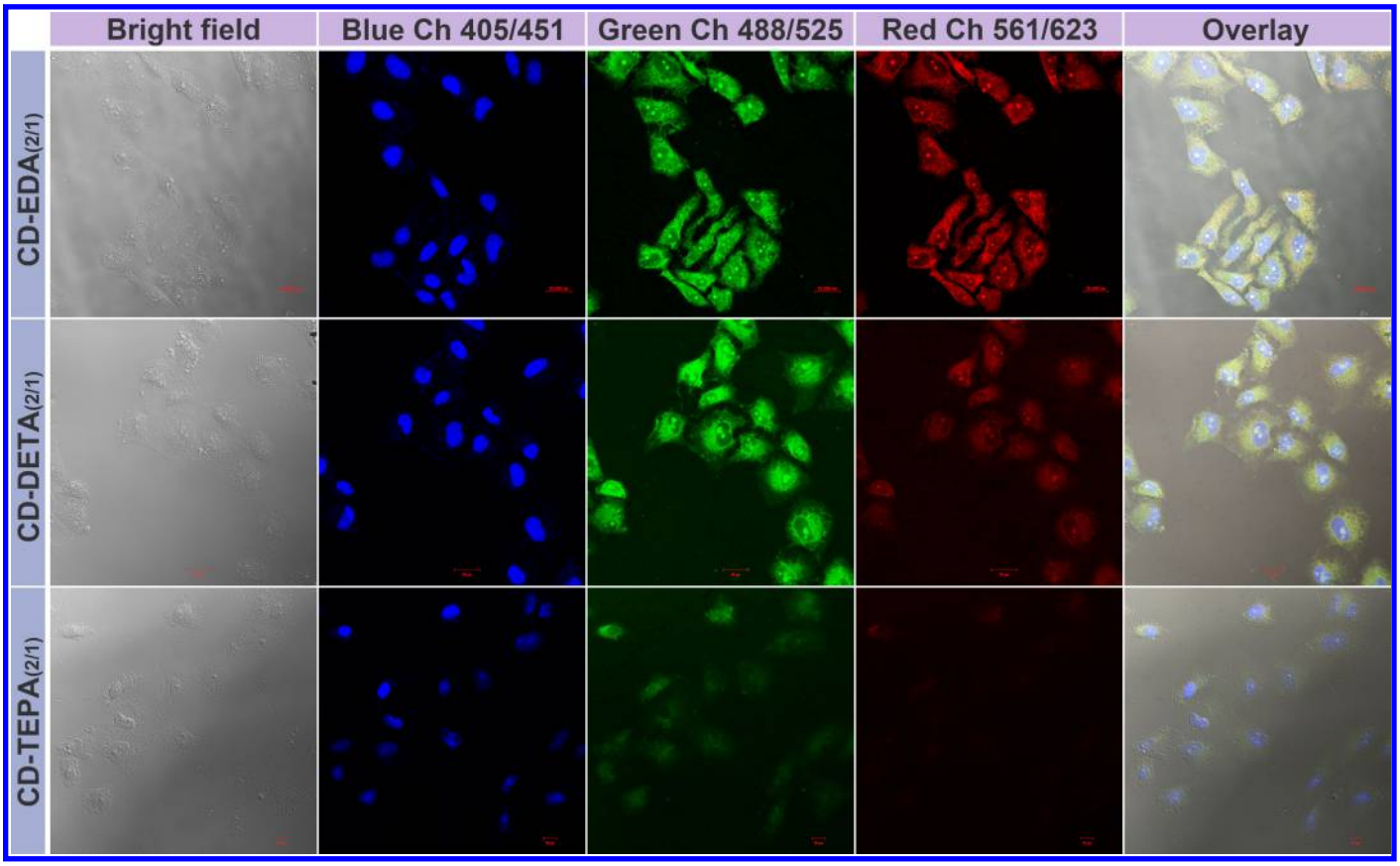

Figure 6. Confocal images of HeLa cells observed under bright field, blue, green, red, and overlay channels. Cells were incubated with 200 µg mL^{-1} in PBS buffer for 4 h and cell nuclei were stained using DAPI.

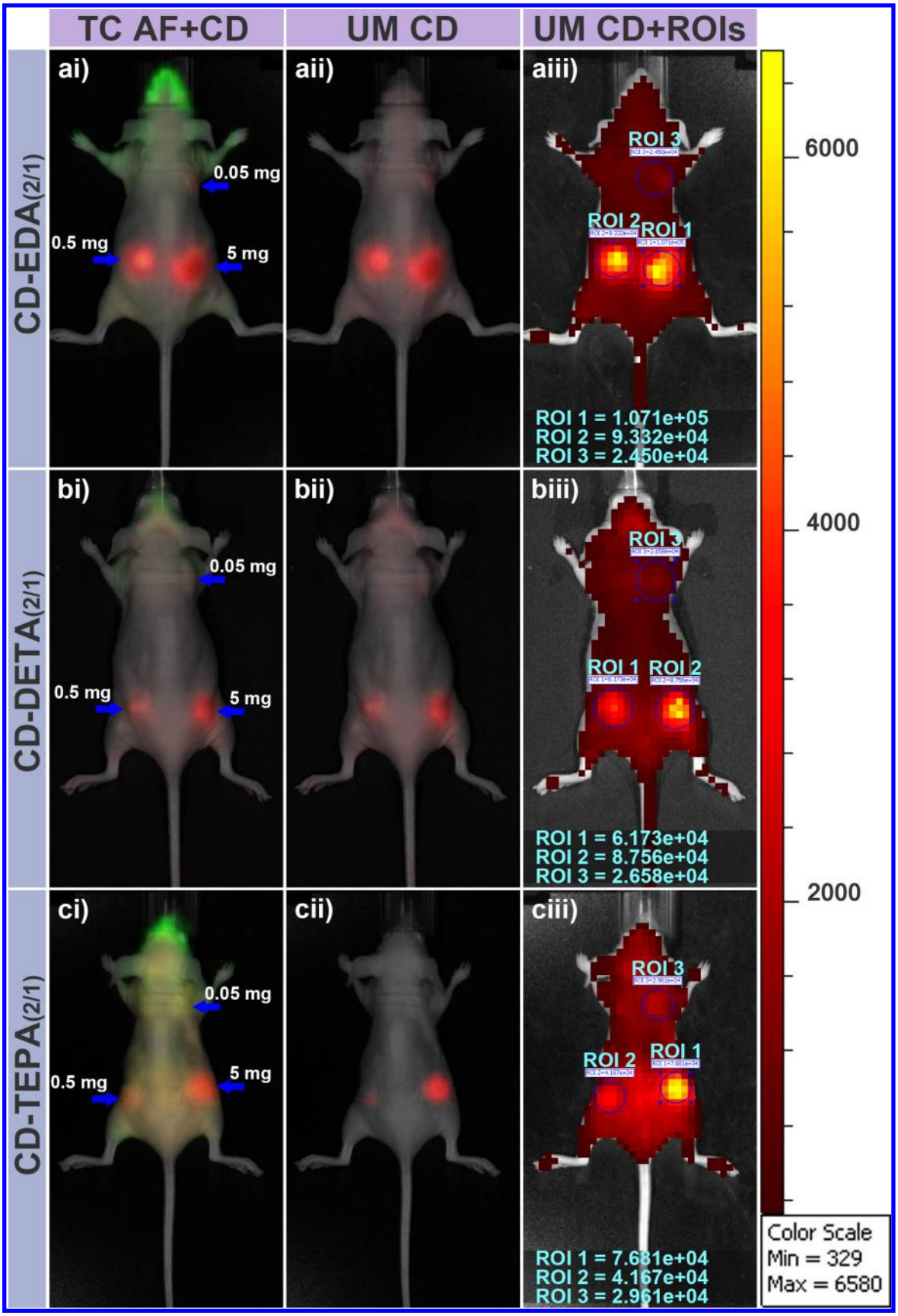

Figure 7. *In-vivo* fluorescence imaging of nude mice injected subcutaneously with **CD-EDA$_{(2/1)}$**, **CD-DETA$_{(2/1)}$** and **CD-TEPA$_{(2/1)}$** at three injection sites (blue arrow) with increased doses. (ai, bi & ci) The true color (TC) fluorescent composite images of CDs fluorescence and autofluorescence (AF) from mice. (aii, bii & cii) unmixed (UM) images of CDs fluorescence. (aiii, biii & ciii) Fluorescent intensities measured in region of interest (ROIs).

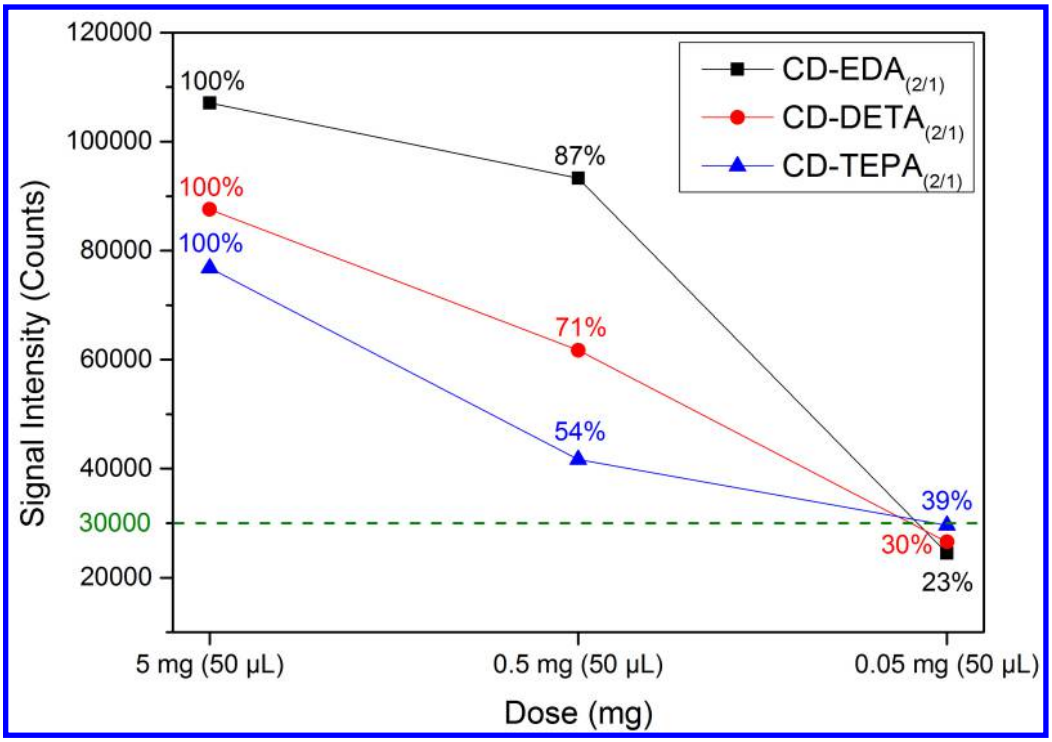

Figure 8. The of the signal intensities of **CD-EDA$_{(2/1)}$**, **CD-DETA$_{(2/1)}$** and **CD-TEPA$_{(2/1)}$** injected at different doses, the percentage of signal attenuation is presented.

Table of contents